

Vibrational anomalies in $A\text{Fe}_2\text{As}_2$ ($A=\text{Ca}$, Sr , and Ba) single crystalsC. C. Homes,^{1,*} Y. M. Dai,² Ana Akrap,³ S. L. Bud'ko,⁴ and P. C. Canfield⁴¹*Condensed Matter Physics and Materials Science Division, Brookhaven National Laboratory, Upton, New York 11973, USA*²*Center for Superconducting Physics and Materials, Department of Physics, Nanjing University, 22 Hankou Road, Nanjing 210093, China*³*DQMP, University of Geneva, CH-1211 Geneva 4, Switzerland*⁴*Ames Laboratory, U.S. DOE, and Department of Physics and Astronomy, Iowa State University, Ames, Iowa 50011, USA*

(Received 12 March 2018; revised manuscript received 1 June 2018; published 2 July 2018)

The detailed behavior of the in-plane infrared-active vibrational modes has been determined in $A\text{Fe}_2\text{As}_2$ ($A = \text{Ca}$, Sr , and Ba) above and below the structural and magnetic transitions at $T_N = 172$, 195 , and 138 K, respectively. Above T_N , two infrared-active E_u modes are observed. In all three compounds, below T_N , the low-frequency E_u mode is observed to split into upper and lower branches; with the exception of the Ba material, the oscillator strength across the transition is conserved. In the Ca and Sr materials, the high-frequency E_u mode splits into an upper and a lower branch; however, the oscillator strengths are quite different. Surprisingly, in both the Sr and Ba materials, below T_N the upper branch appears to be either very weak or totally absent, while the lower branch displays an anomalous increase in strength. The frequencies and atomic characters of the lattice modes at the center of the Brillouin zone have been calculated for the high-temperature phase for each of these materials. The high-frequency E_u mode does not change in position or character across this series of compounds. Below T_N , the E_u modes are predicted to split into features of roughly equal strength. We discuss the possibility that the anomalous increase in the strength of the lower branch of the high-frequency mode below T_N in the Sr and Ba compounds, and the weak (silent) upper branch, may be related to the orbital ordering and a change in the bonding between the Fe and As atoms in the magnetically ordered state.

DOI: [10.1103/PhysRevB.98.035103](https://doi.org/10.1103/PhysRevB.98.035103)**I. INTRODUCTION**

The discovery of superconductivity in the iron-based materials [1] with superconducting critical temperatures (T_c 's) in excess of 50 K [2,3] has prompted an intensive investigation of the physical properties of these multiband materials in an effort to understand the pairing mechanism of the superconductivity [4–8]. The parent compounds are generally paramagnetic metals at room temperature. As the temperature is reduced, they typically undergo a structural and magnetic transition into anti-ferromagnetic (AFM) state, but remain metallic. The $A\text{Fe}_2\text{As}_2$ ($A = \text{Ca}$, Sr , or Ba) materials are particularly interesting; not only do they undergo structural and magnetic transitions, but superconductivity may also be induced through a variety of chemical substitutions, as well as through the application of pressure. The compound CaFe_2As_2 is tetragonal at high temperature; depending on growth conditions, it either undergoes a magnetic and structural transition to an orthorhombic phase with spin-density-wave-like magnetic order at $T_N \simeq 172$ K [9–13], or it undergoes a dramatic decrease of the c -axis lattice parameter and enters into a nonmagnetic, collapsed-tetragonal (cT) phase below 100 K [14,15]; the cT phase, which is unique to this material, may also be stabilized by the application of pressure [16,17] or through chemical substitution on various sites [18–21]. Superconductivity may be induced through either the application of pressure [14,16,22–24], or through chemical substitution, resulting in electron [25–28], hole [29],

or isovalent [19] doping; co-doping with La and P has been reported to yield a critical temperature as high as $T_c \simeq 45$ K [30]. In SrFe_2As_2 , the structural and magnetic transition is observed at a somewhat higher temperature, $T_N \simeq 195$ K [31–33]; superconductivity may be induced through a variety of chemical substitutions [26,34–37], as well as pressure [38,39], with T_c 's in the hole-doped materials as high as $\simeq 37$ K. The structural and magnetic transition in BaFe_2As_2 is lower than what is observed in the other two materials, $T_N \simeq 138$ K [40]; superconductivity may be induced through the application of pressure [38,41–43], or by chemical substitution [23,44–55], with T_c 's as high as $\simeq 40$ K in the hole-doped materials.

As with the cuprates, the proximity of superconductivity to an AFM region suggests that the superconductivity may be mediated by spin fluctuations [56–59], a notion that is supported by the argument that electron-phonon coupling in this class of materials is too small to give rise to the high transition temperatures [60]. However, the behavior of the infrared-active lattice modes can, nonetheless, be quite striking; an example of this is the infrared phonon anomaly in BaFe_2As_2 observed below the structural and magnetic transition [61–65]. In addition, the observation of a large iron isotope effect in several iron-based superconductors suggests an unconventional role for electron-phonon coupling may be possible [66].

In this work we extend our recent investigation of the electronic properties of the $A\text{Fe}_2\text{As}_2$ ($A = \text{Ca}$, Sr , or Ba) parent compounds [67], to include the detailed behavior of the in-plane infrared-active vibrational modes above and below T_N . In each of the materials, two infrared-active E_u modes

*homes@bnl.gov

are observed above T_N . Below the structural and magnetic transition, the low-frequency E_u mode splits into an upper and a lower branch of somewhat different strengths. In the Ca and Sr materials, the oscillator strength is conserved across the transition; however, in the Ba material the strength of this mode appears to weaken slightly below T_N . In the Ca and Sr materials, the high-frequency E_u mode splits into an upper and lower branch below T_N ; the two branches have dramatically different intensities. The oscillator strength is conserved through the transition in the Ca material, but displays an anomalous increase in strength below T_N in the Sr material. In Ba material, the high-frequency E_u mode no longer appears to split below T_N ; instead, it appears to undergo an abrupt decrease in frequency to become the lower branch, with the upper branch now being either very weak or completely absent. Furthermore, the oscillator strength of this mode increases anomalously below T_N [61]. Both the high and low-frequency modes in this material display an asymmetric line shape below the structural and magnetic transition, indicating that the lattice modes may be coupling to spin or charge excitations. The vibrational frequencies and atomic intensities have been calculated at the center of the Brillouin zone for the high-temperature tetragonal phase using an *ab initio* method for the three different compounds. The high-frequency mode involves only in-plane Fe and As displacements that shows little change in frequency or vibrational character across the Ca \rightarrow Sr \rightarrow Ba series. However, the position of the low-frequency mode decreases significantly, with the character of the low-frequency mode shifting from an almost pure alkali-earth mode in the Ca material, to a more mixed character in the Sr and Ba compounds, that includes a significant component from the Fe–As planes. Surprisingly, simple empirical force-constant models predict that both infrared-active E_u modes should split into two new vibrations of roughly equal strength, contrary to what is observed for the high-frequency E_u mode. We consider the possibility that the lack of splitting and the anomalous increase in strength observed in the high-frequency E_u mode below T_N may be related to the orbital ordering and the change in the nature of the bonding between the As and Fe atoms in the magnetically-ordered state.

II. EXPERIMENT

Single crystals of AFe_2As_2 ($A = \text{Ca, Sr, or Ba}$) were grown using conventional high-temperature solution growth techniques either out of self flux ($A = \text{Ba}$) [45], or out of Sn flux ($A = \text{Ca, Sr}$) [9,15,68], and characterized by x-ray scattering, electrical resistivity and magnetic susceptibility measurements. The reflectance of millimeter-sized, as-grown crystal faces has been measured at a near-normal angle of incidence for light polarized in the a - b planes over a wide frequency range from the far infrared ($\simeq 3$ meV) to the ultraviolet ($\simeq 5$ eV) for a wide variety of temperatures above and below T_N using an *in situ* evaporation technique [69]. Only naturally occurring crystal faces have been used; the samples have not been cleaved or polished. The complex conductivity is determined from a Kramers-Kronig analysis of the reflectance [70], the details of which have been discussed in a previous publication [67].

III. RESULTS AND DISCUSSION

A. Fano profile

The vibrational properties of these materials are determined from the symmetry properties of the space group. Above T_N , the three materials studied all crystallize in the tetragonal $I4/mmm$ space group. The irreducible vibrational representation is

$$\Gamma_{\text{HT}} = A_{1g} + B_{1g} + 2E_g + 2A_{2u} + 2E_u,$$

where the E_u and A_{2u} vibrations are infrared active in the a - b planes and along the c axis, respectively. Accordingly, the two infrared active modes observed in these materials at room temperature are assigned as E_u modes. Below T_N , there is a weak structural transition to an orthorhombic $Fmmm$ space group, with the irreducible vibrational representation,

$$\Gamma_{\text{LT}} = A_g + B_{1g} + 2B_{2g} + 2B_{3g} + 2B_{1u} + 2B_{2u} + 2B_{3u},$$

where the B_{1u} modes are active along the c axis, and the orthorhombic distortion lifts the degeneracy of the E_u mode and splits it into $B_{2u} + B_{3u}$ (active along the b and a axes, respectively) for a total of four infrared-active modes at low temperature. However, *ab initio* studies indicate that the splitting of the E_u mode in the related LaFeAsO compound should be relatively small [71], of the order of 1.5 cm^{-1} (0.2 meV).

In the absence of coupling to a continuum of excitations, infrared-active modes usually display a symmetric Lorentzian profile. However, it is possible that coupling to either a spin or charge background may be present, so the infrared-active vibrations have been fit using a phenomenological complex dielectric function, $\tilde{\epsilon} = \epsilon_1 + i\epsilon_2$, for a Fano-shaped Lorentz oscillator [73,74],

$$\tilde{\epsilon}(\omega) = \frac{\Omega_0^2}{\omega_0^2 - \omega^2 - i\gamma_0\omega} \left(1 + i\frac{\omega_q}{\omega}\right)^2 + \left(\frac{\Omega_0\omega_q}{\omega_0\omega}\right)^2, \quad (1)$$

where ω_0 , γ_0 , and Ω_0 are the position, width, and strength of the vibration, respectively, and the asymmetry is described by the dimensionless parameter $1/q = \omega_q/\omega_0$. The complex conductivity is $\tilde{\sigma}(\omega) = \sigma_1 + i\sigma_2 = -2\pi i\omega[\tilde{\epsilon}(\omega) - \epsilon_\infty]/Z_0$ (in units of $\Omega^{-1} \text{ cm}^{-1}$); $Z_0 \simeq 377 \Omega$ is the impedance of free space. The complex conductivity satisfies $\tilde{\sigma}^*(\omega) = \tilde{\sigma}(-\omega)$. The real and imaginary parts of the optical conductivity are then

$$\sigma_1(\omega) = \frac{2\pi}{Z_0} \frac{\Omega_0^2[\gamma_0\omega^2 - 2(\omega^2\omega_0 - \omega_0^3)/q - \gamma_0\omega_0^2/q^2]}{(\omega^2 - \omega_0^2)^2 + \gamma_0^2\omega^2} \quad (2)$$

and

$$\begin{aligned} \sigma_2(\omega) &= \frac{2\pi}{Z_0} \frac{\omega\Omega_0^2[(\omega^2 - \omega_0^2) - 2\gamma_0\omega_0/q + (\omega^2 - \omega_0^2 + \gamma_0^2)/q^2]}{(\omega^2 - \omega_0^2)^2 + \gamma_0^2\omega^2}. \end{aligned} \quad (3)$$

Note that for finite ω_0 , in the $\omega_q \rightarrow 0$ (or $1/q^2 \rightarrow 0$) limit, the dielectric function for a simple Lorentz oscillator is recovered; however, as $1/q^2$ increases the line shape becomes increasingly asymmetric.

The infrared-active modes are superimposed on an electronic background, which in our previous study of these

TABLE I. The experimental and calculated (relaxed) lattice constants and atomic fractional coordinates of $A\text{Fe}_2\text{As}_2$ ($A = \text{Ca}, \text{Sr}, \text{and Ba}$) for the nonmagnetic high-temperature tetragonal ($I4/mmm$) phase. The fractional coordinates for the A and Fe atoms are $(0\ 0\ 0)$ and $(0\ \frac{1}{2}\ \frac{1}{4})$, respectively.

Cell parameters	CaFe_2As_2		SrFe_2As_2		BaFe_2As_2	
	Experiment ^a	DFT	Experiment ^b	DFT	Experiment ^c	DFT
a (Å)	3.872	3.880	3.927	3.897	3.964	3.964
c (Å)	11.73	11.49	12.37	12.27	13.02	12.64
c/a	3.029	2.962	3.150	3.057	3.285	3.187
As $(0\ 0\ z)$	0.3612	0.3587	0.361	0.3528	0.361	0.3463
Fe-As (Å)	2.369	2.308	2.396	2.321	2.452	2.326
As-Fe-As ($^\circ$)	109.6	114.5	110.1	115.7	107.8	116.9

^aReference [72].

^bReference [31].

^cReference [40].

materials [67] was modeled using the two-Drude model [75],

$$\tilde{\epsilon}(\omega) = \epsilon_\infty - \sum_{j=1}^2 \frac{\omega_{p,D;j}^2}{\omega^2 + i\omega/\tau_{D,j}} + \sum_k \frac{\Omega_k^2}{\omega_k^2 - \omega^2 - i\omega\gamma_k}, \quad (4)$$

where ϵ_∞ is the contribution to the real part of the dielectric function from high-frequency excitations. In the first sum, $\omega_{p,D;j}^2 = 4\pi n_j e^2/m_j^*$ and $1/\tau_{D,j}$ are the square of the plasma frequency and scattering rate for the delocalized (Drude) carriers in the j th band, respectively, and n_j and m_j^* are the carrier concentration and effective mass. In the second summation, ω_k , γ_k , and Ω_k are the position, width, and strength of the k th vibration or bound excitation.

B. Lattice dynamics

The electronic properties of $A\text{Fe}_2\text{As}_2$ ($A = \text{Ca}, \text{Sr}, \text{and Ba}$) for the nonmagnetic high-temperature tetragonal ($I4/mmm$) phase have been calculated using density functional theory (DFT) with the generalized gradient approximation (GGA) using the full-potential linearized augmented plane-wave (FP-LAPW) method [76] with local-orbital extensions [77] in the WIEN2K implementation [78]. An examination of different

Monkhorst-Pack k -point meshes indicated that a $5 \times 5 \times 5$ k -point mesh with $R_{\text{mt}}k_{\text{max}} = 8$ was sufficient for good energy convergence. Beginning with the experimental unit cell, the lattice parameters are adjusted and the total energy calculated for each structure; the lowest total energy in this phase space corresponds to the most stable geometry. The atomic fractional coordinates were then relaxed with respect to the total force, typically resulting in residual forces of less than 0.1 mRy/a.u. per atom. This procedure was repeated until no further improvement was obtained. A comparison of the experimental and calculated (relaxed) unit cell parameters is shown in Table I. While the calculated results for the a axis are in excellent agreement with the experimentally determined values, the c axis is systematically smaller, a result that has been noted in other works [79,80].

The phonons have been determined using the direct method, also known as the frozen-phonon technique. To determine the phonons at the zone center, a $1 \times 1 \times 1$ supercell is sufficient. To obtain a complete set of Hellmann-Feynman forces, a total of six independent displacements are required; because there are always some residual forces at the atomic sites we have considered symmetric displacements, which doubles this number, resulting in a total of 12 atomic displacements.

TABLE II. Calculated frequencies and atomic intensities of $A\text{Fe}_2\text{As}_2$ ($A = \text{Ca}, \text{Sr}, \text{and Ba}$) for the zone-center modes in the nonmagnetic high-temperature tetragonal ($I4/mmm$) phase compared with experimentally observed values.

Mode	CaFe_2As_2			SrFe_2As_2			BaFe_2As_2								
	ω_{exp} (cm^{-1})	ω_{calc} (cm^{-1})	Atomic intensity Ca Fe As			ω_{exp} (cm^{-1})	ω_{calc} (cm^{-1})	Atomic intensity Sr Fe As			ω_{exp} (cm^{-1})	ω_{calc} (cm^{-1})	Atomic intensity Ba Fe As		
E_g	—	323	0.00	0.73	0.27	264 ^c	316	0.00	0.72	0.28	264 ^a	313	0.00	0.70	0.30
E_u	264 ^a	300	0.00	0.56	0.44	257 ^a	296	0.00	0.56	0.44	258 ^a	296	0.00	0.55	0.45
A_{2u}	—	279	0.00	0.58	0.42	—	277	0.00	0.59	0.41	—	280	0.00	0.59	0.41
B_{1g}	211 ^b	211	0.00	1.00	0.00	204 ^c	229	0.00	1.00	0.00	217 ^d	232	0.00	1.00	0.00
A_{1g}	189 ^b	207	0.00	0.00	1.00	182 ^c	212	0.00	0.00	1.00	183 ^d	210	0.00	0.00	1.00
E_g	—	142	0.00	0.27	0.73	114 ^c	142	0.00	0.28	0.72	131 ^d	140	0.00	0.30	0.70
E_u	143 ^a	131	0.87	0.07	0.06	109 ^a	102	0.75	0.12	0.13	94 ^a	89	0.66	0.17	0.17
A_{2u}	—	126	0.87	0.05	0.08	—	104	0.75	0.09	0.16	—	95	0.66	0.13	0.21

^aThis work; positions determined just above T_N .

^bReference [11]; the A_{1g} (A_g) and B_{1g} modes are only observed below T_N .

^cReference [81].

^dReferences [82,83]; the A_{1g} (A_g) mode is only observed below T_N .

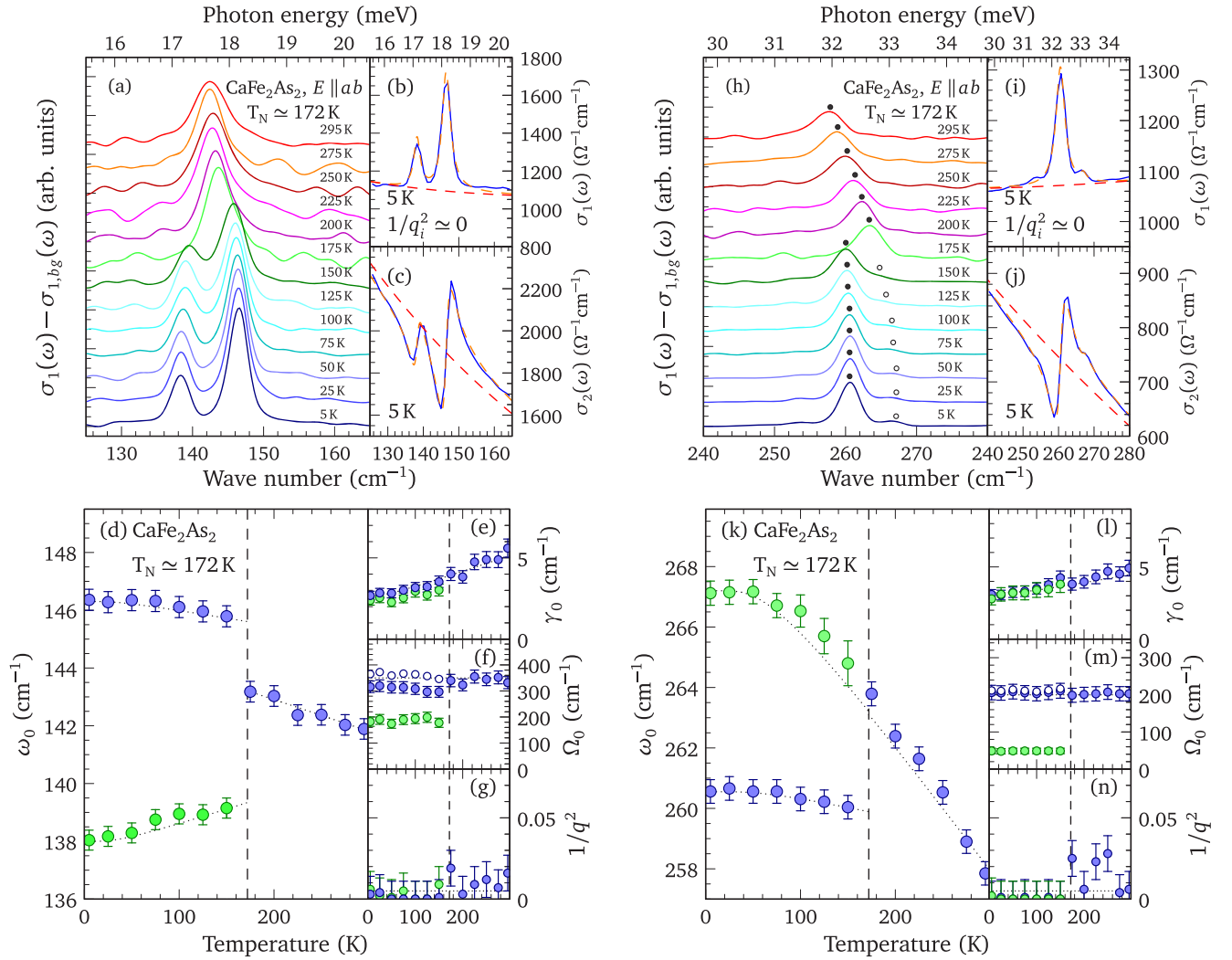


FIG. 1. (a) The temperature dependence of the low-frequency E_u mode in the optical conductivity for CaFe_2As_2 ($T_N \approx 172$ K) with the electronic background removed. (b) The results of the fit at 5 K to the real part of the optical conductivity, and (c) the imaginary part. The temperature dependence of the (d) positions, (e) linewidths, (f) strength of the modes (for $T < T_N$, the open circles are the strengths of the two modes added in quadrature), and (g) asymmetry parameters. (h) The temperature dependence of the high-frequency E_u mode in the optical conductivity with the electronic background removed; the position of the fundamental is indicated by solid circles, below T_N the position of the upper band is denoted by the open circles. (i) The results of the fit at 5 K to the real part of the optical conductivity, and (j) the imaginary part. The temperature dependence of the (k) positions, (l) linewidths, (m) strength of the modes (for $T < T_N$, the open circles are the strengths of the two modes added in quadrature), and (n) asymmetry parameters. Unless otherwise indicated in the text, the dotted lines are drawn as a guide to the eye.

In this case, displacement amplitudes of 0.02 \AA were used. Typical values for the displacements range from 0.02 to 0.06 \AA ; however, because of the highly-distorted nature of the Fe–As planes, a smaller displacement was chosen to ensure that the response was still linear. Due to the lower symmetry in these calculations an $8 \times 8 \times 2$ k -point mesh was used. The calculations have converged when the successive changes for the forces on each atom are less than 0.02 mRy/a.u. The residual forces are collected for each set of symmetric displacements and a list of the Hellmann-Feynman forces are generated. Using the program PHONON [84] the cumulative force constants deconvoluted from the Hellmann-Feynman forces are introduced into the dynamical matrix, which is then diagonalized in order to obtain the phonon frequencies. The atomic intensities are further calculated to describe the

character of the vibration; in this case the intensity refers to the square of the vibrational amplitude of each atom for a given mode. The results are shown in Table II. A general result in these materials is that calculations based on relaxed unit cells tend to return frequencies that are, for the most part, larger than the experimentally-observed energies [85,86]. While better agreement with experiment may be achieved if the experimental values for the unit cell parameters are used [80,86,87], this approach is not recommended because of the large residual forces that may be present in an unrelaxed unit cell.

C. CaFe_2As_2

The real part of the optical conductivity of CaFe_2As_2 is shown in Fig. 1(a) for light polarized in the a - b planes,

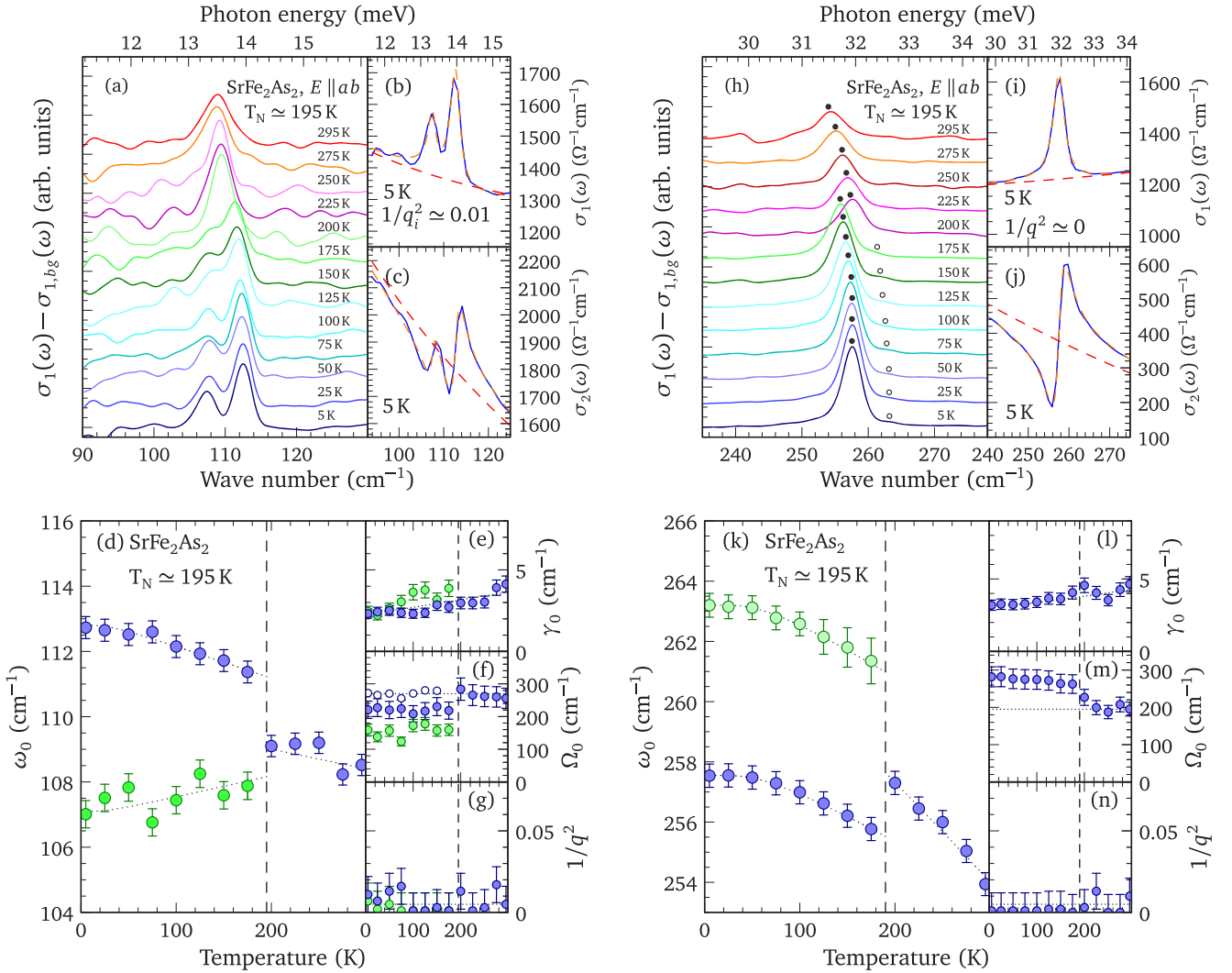


FIG. 2. (a) The temperature dependence of the low-frequency E_u mode in the optical conductivity for SrFe_2As_2 ($T_N \simeq 195$ K) with the electronic background removed. (b) The results of the fit at 5 K to the real part of the optical conductivity, and (c) the imaginary part. The temperature dependence of the (d) positions, (e) linewidths, (f) strength of the modes (for $T < T_N$, the open circles are the strengths of the two modes added in quadrature), and (g) asymmetry parameters. (h) The temperature dependence of the high-frequency E_u mode in the optical conductivity with the electronic background removed; the position of the fundamental is indicated by solid circles, below T_N the position of the upper band is denoted by the open circles. (i) The results of the fit at 5 K to the real part of the optical conductivity, and (j) the imaginary part. The temperature dependence of the (k) position, (l) linewidth, (m) oscillator strength, and (n) asymmetry parameter. Unless otherwise indicated in the text, the dotted lines are drawn as a guide to the eye.

with the electronic background removed, in the region of the low-frequency E_u mode at $\simeq 142$ cm⁻¹ (the curves have been offset for clarity). At room temperature, only one mode may be observed; below T_N , this mode clearly splits into two features at $\simeq 138$ and 146 cm⁻¹ in response to the orthorhombic distortion, in agreement with a previous study [65]. The fit to the real and imaginary parts of the optical conductivity at 5 K is shown in Figs. 1(b) and 1(c), respectively, using the Fano line shapes in Eqs. (2) and (3) with an electronic background described by the two-Drude model; the line shapes are reproduced quite well. The position of the low-frequency E_u mode is gradually increasing with decreasing temperature until it splits below T_N ; the upper branch increases slightly in frequency (hardens), while the lower branch decreases (softens) as the temperature is lowered, shown in Fig. 1(d). We adopt the scheme of applying

the color of the fundamental to track the strongest feature below T_N . The linewidth shown in Fig. 1(e) is decreasing with temperature; below T_N there is no discontinuity as the widths of the new modes are roughly equal and continue to decrease with temperature. Below T_N , the oscillator strength of the lower branch is less than that of the upper branch [reflected in the color scheme of Fig. 1(d)]. Individually, the strengths of these modes are less than that of the high-temperature mode, but if the strengths are added in quadrature, that is, $\Omega_1^2 + \Omega_2^2$, then they reproduce the strength of the original E_u mode, as shown in Fig. 1(f). The small value of the asymmetry parameter in Fig. 1(g) indicates that the modes are all symmetric, both above and below T_N .

The optical conductivity is shown with the electronic background removed in Fig. 1(h) in the region of the high-frequency

E_u mode at $\simeq 258 \text{ cm}^{-1}$ (the curves have been offset for clarity). At room temperature, a single mode is observed; below T_N , two new modes appear at $\simeq 261$ and 267 cm^{-1} ; the fit to the real and imaginary parts of the optical conductivity at 5 K using two oscillators reproduces the data quite well, as shown in Figs. 1(i) and 1(j), respectively. In general, while there are a number of other weak features in Figs. 1(a) and 1(h) that might be argued to be due to vibrational structure, we limit our attention to only those features that show a systematic temperature dependence. Above T_N the frequency of the E_u mode increases relatively quickly with decreasing temperature; below T_N , this mode appears to continue as a very weak upper branch that continues to harden, while the fundamental undergoes an abrupt decrease in frequency to form a strong lower branch that hardens slightly with decreasing temperature, shown in Fig. 1(k). Interestingly, the dotted line connecting the fundamental above T_N to the weak upper branch below T_N is the expected behavior for a symmetric anharmonic decay into two acoustic modes with identical frequencies and opposite momenta [86,88,89]. The width of the mode shown in Fig. 1(l) is decreasing with temperature; below T_N , the width of the upper and lower branches are similar, and both continue to decrease with temperature; the dotted line again indicates the behavior expected from an anharmonic decay scheme. The strength of the upper branch is much less than that of the lower branch, as shown in Fig. 1(m), but once again when the oscillator strengths are added in quadrature then they reproduce the strength of the E_u mode at high temperature. The asymmetry parameter in Fig. 1(n) indicates that the modes are symmetric, both above and below T_N .

The frequencies of the zone-center lattice vibrations have been calculated for the nonmagnetic high-temperature tetragonal phase of CaFe_2As_2 (Sec. III B). The position of the experimentally-observed low-frequency E_u mode at $\simeq 143 \text{ cm}^{-1}$, measured just above T_N , is in good agreement with the calculated value of 131 cm^{-1} ; the atomic intensities indicate that this mode involves mainly the Ca atom, with only minor contributions from the Fe and As atoms. At 300 cm^{-1} , the calculated position of the high-frequency E_u mode is larger the experimentally-observed value of 264 cm^{-1} ; the atomic intensities indicate that this in-plane mode involves roughly equal contributions from the Fe and As atoms, with no contribution from the Ca atom (Table II).

D. SrFe_2As_2

The real part of the optical conductivity of SrFe_2As_2 is shown in Fig. 2(a) for light polarized in the a - b planes, with the electronic background removed, in the region of the low-frequency E_u mode at $\simeq 109 \text{ cm}^{-1}$ (the curves have been offset for clarity). At room temperature, only a single mode is observed; this crystal is somewhat smaller than the other two, consequently the data are slightly noisier in the long-wavelength region. Below $T_N \simeq 195 \text{ K}$ this mode clearly splits into two features at $\simeq 107$ and 112 cm^{-1} . Using the previously described approach, the Fano line shape is fit to the real and imaginary parts of the optical conductivity at 5 K as shown in Figs. 2(b) and 2(c), respectively; the line shapes are reproduced quite well. As a result of the rather large value for T_N in this material, the position of the low-frequency E_u mode shows

relatively little temperature dependence before splitting abruptly below the structural and magnetic transition; the upper branch continues to harden with decreasing temperature, while the lower branch softens, shown in Fig. 2(d). The linewidth shown in Fig. 2(e) is decreasing with temperature; below T_N there is no discontinuity as the widths of the new modes are roughly equal and continue to decrease with temperature. Below T_N the oscillator strength of the lower branch is less than that of the upper branch, but if the strengths of these two modes are added in quadrature, they reproduce the strength of the fundamental mode, as shown in Fig. 2(f). The asymmetry parameter in Fig. 2(g) indicates that the modes are all symmetric, both above and below T_N .

The optical conductivity is shown with the electronic background removed in Fig. 2(h) in the region of the high-frequency E_u mode at $\simeq 254 \text{ cm}^{-1}$ (the curves have been offset for clarity). For $T \ll T_N$, there is some evidence that this mode splits, but the shoulder just above the main peak is extremely weak and difficult to refine. As a consequence, we have used only a single oscillator to fit the data, while estimating the position of the shoulder from the peak in the conductivity (the width and oscillator strength of this feature are not reported). The fit to the real and imaginary parts of the optical conductivity at 5 K using the Fano line shape reproduces the data quite well, as shown in Figs. 2(i) and 2(j), respectively. Above T_N , the position of this mode hardens with decreasing temperature before splitting below T_N into a strong lower branch and a weak upper branch, both of which continue to harden with decreasing temperature, shown in Fig. 2(k). The width of the mode shown in Fig. 2(l) is decreasing continuously with temperature and shows no anomalous behavior at T_N . The temperature dependence of the frequency and position is consistent with the anharmonic decay scheme (dotted lines). Above T_N , the strength of this mode is identical to that observed in CaFe_2As_2 ; however, below T_N , this mode displays an unusual increase in strength. The asymmetry parameter in Fig. 2(n) indicates that the mode is symmetric, both above and below T_N .

The calculated position of the high-frequency E_u mode for SrFe_2As_2 in the tetragonal phase of 296 cm^{-1} is once again larger than the experimentally observed position at 257 cm^{-1} (taken just above T_N); however, the nature of this mode is unchanged from CaFe_2As_2 with nearly identical atomic intensities (Table II). The calculated position of the low-frequency E_u mode of 102 cm^{-1} is in reasonable agreement with the experimentally observed value of 109 cm^{-1} ; however, this value is significantly lower than it is in CaFe_2As_2 (102 compared to 131 cm^{-1}), and the character of this mode is altered with the Sr atom now playing a decreased role, with larger contributions from the Fe and As atoms.

E. BaFe_2As_2

The real part of the optical conductivity of BaFe_2As_2 is shown in Fig. 3(a), with the electronic background removed, in the region of the low-frequency E_u mode at $\simeq 94 \text{ cm}^{-1}$ (the curves have been offset for clarity). As in the other two cases, at room temperature a single mode is observed; below T_N , it splits into two modes at $\simeq 93$ and 97 cm^{-1} . Using the previously described approach, the Fano line shape is fit to the real and

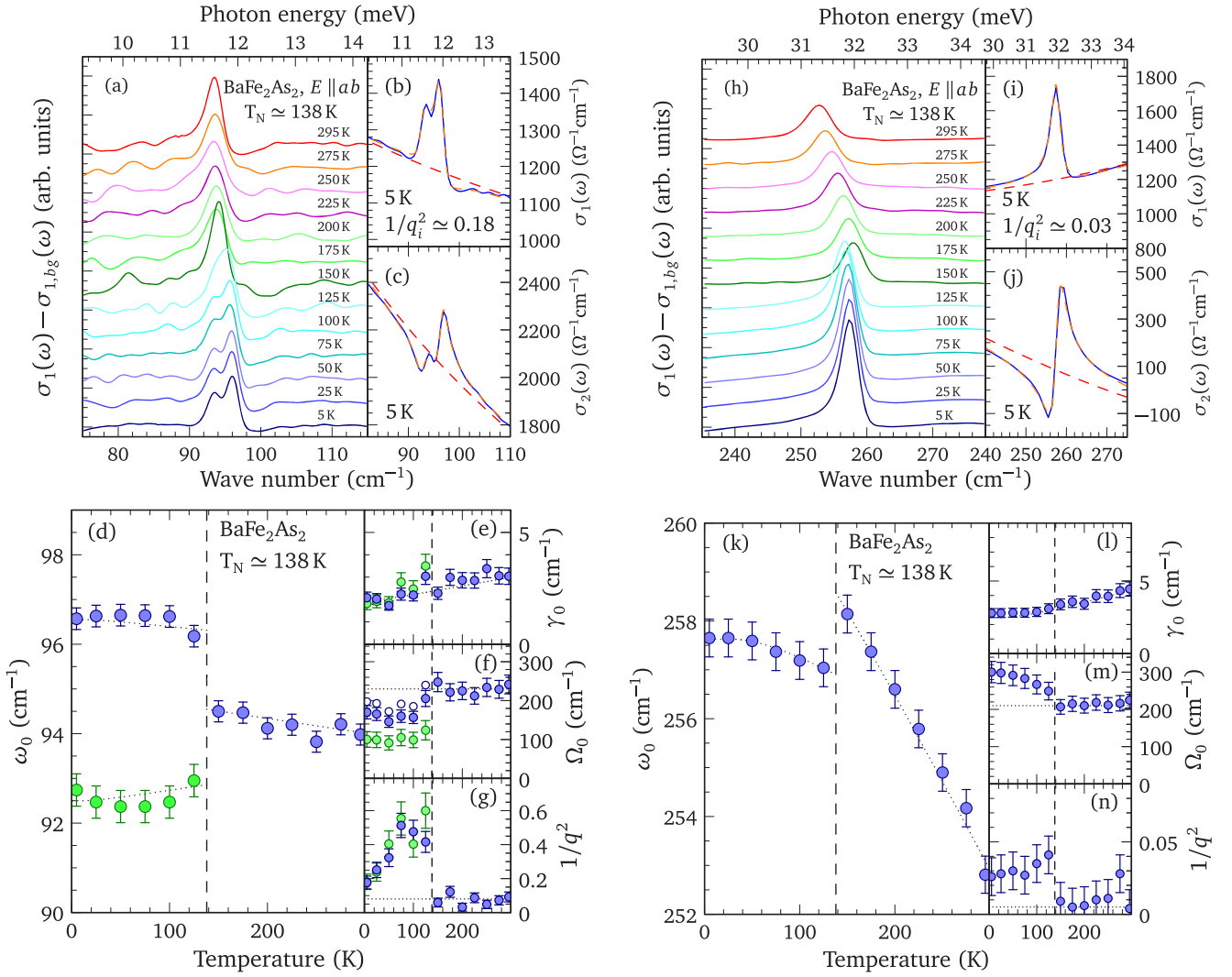


FIG. 3. (a) The temperature dependence of the low-frequency E_u mode in the optical conductivity for BaFe_2As_2 ($T_N \simeq 138$ K) with the electronic background removed. (b) The results of the fit at 5 K to the real part of the optical conductivity, and (c) the imaginary part. The temperature dependence of the (d) positions, (e) linewidths, (f) strength of the modes (for $T < T_N$, the open circles are the strengths of the two modes added in quadrature), and (g) asymmetry parameters. (h) The temperature dependence of the high-frequency E_u mode in the optical conductivity with the electronic background removed. (i) The results of the fit at 5 K to the real part of the optical conductivity, and (j) the imaginary part. The temperature dependence of the (k) position, (l) linewidth, (m) oscillator strength, and (n) asymmetry parameter. Unless otherwise indicated in the text, the dotted lines are drawn as a guide to the eye.

imaginary parts of the optical conductivity at 5 K and is shown in Figs. 3(b) and 3(c), respectively, reproducing the data quite well. The position of the low-frequency E_u mode above and below T_N is shown in Fig. 3(d); overall, this mode shows little frequency dependence, in agreement with a previous study [64]. The line width shown in Fig. 3(e) is decreasing with temperature; below T_N there is no discontinuity as the widths of the new modes are roughly equal and continue to decrease with temperature. Below T_N , the oscillator strength of the lower branch is less than that of the upper branch. Unlike the other two materials, when the strengths of the two modes are added in quadrature, they fail to reproduce the strength of the fundamental mode, as shown in Fig. 3(f). The asymmetry parameter in Fig. 3(g) indicates this mode is symmetric at high temperature; however, below T_N , both modes display a pronounced asymmetry.

The optical conductivity is shown with the electronic background removed in Fig. 3(h) in the region of the high-frequency E_u mode at $\simeq 254$ cm^{-1} (the curves have been offset for clarity). At high temperature, a single mode is observed; below T_N , unlike the previous two materials, we fail to observe an unambiguous splitting. Other workers have observed a weak shoulder in optical conductivity at $\simeq 262$ cm^{-1} , which they attribute to the splitting of this mode [64]; however, we consider only a single oscillator. The fit to the real and imaginary parts of the optical conductivity at 5 K using the Fano line shape reproduces the data quite well, as shown in Figs. 3(i) and 3(j), respectively. The position of this mode hardens with decreasing temperature until it softens anomalously at T_N before continuing to harden slightly at low temperature. The softening is understood as a splitting in response to the orthorhombic distortion in which the upper branch is curiously

silent. The width of the mode, shown in Fig. 3(l), decreases with temperature, showing no discontinuity at T_N . The temperature dependence of the frequency and position are both consistent with the anharmonic decay scheme (dotted lines). Above T_N , the strength of this mode is identical to that observed in the other two materials; however, below T_N , this mode increases dramatically in strength, shown in Fig. 3(m). The asymmetry parameter in Fig. 3(n) indicates that the mode is symmetric above T_N , but develops a slight asymmetry at low temperature.

The calculated position of the low-frequency E_u mode at 89 cm^{-1} is in good agreement with the experimentally observed position at $\simeq 94 \text{ cm}^{-1}$; however, in a continuation of the trend observed in SrFe_2As_2 , the character of this mode has changed significantly with the Ba atom now playing a reduced role with increased contributions from the Fe and As atoms (Table II). The calculated position of the high-frequency mode of 298 cm^{-1} is larger than the experimentally observed value at 258 cm^{-1} ; interestingly, the vibrational character for this mode remains unchanged across all three materials.

F. Phonon anomalies

In AFe_2As_2 , the series of $A = \text{Ca, Sr, and Ba}$ represents the steadily increasing size of the alkali earth atom, which is reflected by the increase in the c -axis lattice parameter (Table I). The vibrational properties of CaFe_2As_2 are an interesting point of departure in that they may be described as more or less conventional; both E_u modes harden with decreasing temperature as expected [86,88,89] and the $E_u \rightarrow B_{2u} + B_{3u}$ splitting is observed below T_N for both modes. While one mode is typically stronger than the other, when the strengths of the modes are added in quadrature, the strength of the original E_u mode is recovered. It is not unusual for the strengths of the B_{2u} and B_{3u} modes to be different; however, in the case of the high-frequency E_u mode, they are significantly different, $\Omega_2^2/\Omega_1^2 \simeq 0.05$ [Fig. 1(m)]. This is rather surprising as a simple empirical force-constant model [90] that reproduces the positions of the vibrations below T_N indicates that while there is some difference in the strengths of the low-frequency modes, the strengths of the high-frequency B_{2u} and B_{3u} modes should be nearly identical. In SrFe_2As_2 , the low-frequency E_u mode hardens with decreasing temperature and underdoes a $B_{2u} + B_{3u}$ splitting below T_N ; the oscillator strength is conserved. Beyond this point, any similarity with the Ca compound vanishes; while the high-frequency E_u mode appears to split below T_N , the response is dominated by the lower branch, while the shoulder that comprises the upper branch is extremely weak. In addition, the strength of the lower branch is observed to increase anomalously below T_N [Fig. 2(m)] by nearly a factor of two.

The most striking phonon anomalies occur in BaFe_2As_2 . While the splitting of the low-frequency E_u mode is observed below T_N [64], the strengths of the new modes now sum to less than the original E_u mode [Fig. 3(f)]. Additionally, both modes appear to have asymmetric line shapes; considering that these modes have an increased Fe and As atomic character, the possibility of lattice mode coupling to spin or charge excitations within the conducting Fe–As planes can not be

discounted. Furthermore, the high-frequency E_u mode fails to demonstrate any splitting below T_N and undergoes a dramatic increase in oscillator strength of $\simeq 2.3$ [61,64]. Below T_N , the spins order antiferromagnetically along the a axis and ferromagnetically along the b axis [10,91]. Optical studies of mechanically-detwinned single crystals of this compound indicate that there is a significant optical anisotropy with the optical conductivity along the a axis being roughly twice that along the b axis over much of the infrared region [63,92,93]. The high-frequency mode is only observed along the b axis below T_N , and is thus a B_{2u} mode [63]. The absence of the B_{3u} mode has been attributed to screening effects [64]; however, given that the conductivity anisotropy in the region of the mode is only about a factor of two, screening seems unlikely [94].

The bonding in the highly-distorted Fe–As planes occurs from the hybridization of the Fe d_{xz} and d_{yz} and As $4p$ orbitals [95,96]; below T_N , there is a strongly orbital-dependent reconstruction of the electronic structure [97–99], resulting in orbital ordering [100–107]. In this scenario, degeneracy between the d_{xz} and d_{yz} orbitals is removed, resulting in unequal occupations. The strength of an infrared-active mode is calculated from the Born effective charge on the atoms, which when taken with the atomic displacements for a particular normal mode, is used to calculate the strength of the dipole moment. Changes in the strength of a mode require changes in either bonding or coordination; the weak nature of the structural phase transition rules out the latter, leaving only changes in bonding as a reasonable explanation. Because there is a quasi-one-dimensional spin-density wave (SDW) along the a axis, it is possible that a weak spin-dimerization could result in a weak bond-centered charge-density wave (CDW) in this direction as well with twice the periodicity of the SDW. Furthermore, we speculate that the different charge densities associated with the bonds may result in dramatically different dipole moments along the a and b directions in the magnetically-ordered state, resulting in the increase in strength of the B_{2u} mode and the almost total extinction of the B_{3u} mode.

IV. CONCLUSIONS

The detailed temperature dependence of the in-plane infrared active modes has been studied in AFe_2As_2 ($A = \text{Ca, Sr, and Ba}$) above and below the structural and magnetic transitions at $T_N = 172, 195, \text{ and } 138 \text{ K}$, respectively. The phonon frequencies and atomic characters have also been determined from first principles for each compound in the high-temperature tetragonal phase. The CaFe_2As_2 material is the most conventional; the $E_u \rightarrow B_{2u} + B_{3u}$ splitting into upper and lower branches is observed below T_N for both of the infrared-active modes. For the low-frequency E_u mode, below T_N the lower branch continues to soften with decreasing temperature, while the upper branch hardens. The high-frequency E_u mode splits into upper and lower branches of very different strengths, both of which continue to harden with decreasing temperature in a fashion consistent with an anharmonic decay scheme. For both modes, the oscillator strengths are conserved

across the transition, and none of the modes shows any obvious asymmetry. The behavior of the low-frequency E_u mode is similar in SrFe_2As_2 ; however, while the high-frequency E_u mode is still observed to split in this material, the upper branch is now extremely weak, and the oscillator strength of the lower branch increases anomalously below T_N . This behavior is repeated in BaFe_2As_2 , except that now the oscillator strengths of the low-frequency modes are no longer conserved; below T_N , the high-frequency E_u mode softens anomalously into a lower branch (B_{2u}) [63] that increases dramatically in strength with decreasing temperature, while the upper branch (B_{3u}) is now entirely absent. The presence of a SDW (and possibly a weak CDW) along the a axis below T_N suggests that the nature of the bonding along the a and b axis has been altered due to orbital ordering, which may be responsible for the increase in the strength of the B_{2u} mode and the almost total extinction of the B_{3u} mode.

ACKNOWLEDGMENTS

We would like to acknowledge useful discussions with S. V. Dordevic, N. Felix, and R. Yang. Work at the Ames Laboratory (S.L.B. and P.C.C.) was supported by the U.S. Department of Energy (DOE), Office of Science, Basic Energy Sciences, Materials Sciences and Engineering Division. The Ames Laboratory is operated for the U.S. Department of Energy by Iowa State University under Contract No. DE-AC02-07CH11358. We would like to thank A. Thaler and S. Ran for help with sample synthesis. A.A. acknowledges funding from The Ambizione Fellowship of the Swiss National Science Foundation. This work was performed in part at the Aspen Center for Physics, which is supported by National Science Foundation Grant PHY-1066293. Work at Brookhaven National Laboratory was supported by the Office of Science, U.S. Department of Energy under Contract No. DE-SC0012704.

-
- [1] Y. Kamihara, T. Watanabe, M. Hirano, and H. Hosono, Iron-based layered superconductor $\text{La}[\text{O}_{1-x}\text{F}_x]\text{FeAs}$ ($x = 0.05-0.12$) with $T_c = 26$ K, *J. Am. Chem. Soc.* **130**, 3296 (2008).
- [2] Z.-A. Ren, J. Yang, W. Lu, W. Yi, X.-L. Shen, Z.-C. Li, G.-C. Che, X.-L. Dong, L.-L. Sun, F. Zhou, and Z.-X. Zhao, Superconductivity in the iron-based F-doped layered quaternary compound $\text{Nd}[\text{O}_{1-x}\text{F}_x]\text{FeAs}$, *Europhys. Lett.* **82**, 57002 (2008).
- [3] R. Z.-An, L. Wei, Y. Jie, Y. Wei, S. Xiao-Li, Zheng-Cai, C. Guang-Can, D. Xiao-Li, S. Li-Ling, Z. Fang, and Z. Zhong-Xian, Superconductivity at 55 K in iron-based F-doped layered quaternary compound $\text{Sm}[\text{O}_{1-x}\text{F}_x]\text{FeAs}$, *Chin. Phys. Lett.* **25**, 2215 (2008).
- [4] D. C. Johnston, The puzzle of high temperature superconductivity in layered iron pnictides and chalcogenides, *Adv. Phys.* **59**, 803 (2010).
- [5] J. Paglione and R. L. Greene, High-temperature superconductivity in iron-based materials, *Nat. Phys.* **6**, 645 (2010).
- [6] P. C. Canfield and S. L. Bud'ko, FeAs-based superconductivity: A case study of the effects of transition metal doping on BaFe_2As_2 , *Annu. Rev. Condens. Matter Phys.* **1**, 27 (2010).
- [7] D. S. Inosov, Spin fluctuations in iron pnictides and chalcogenides: From antiferromagnetism to superconductivity, *C. R. Phys.* **17**, 60 (2016).
- [8] Q. Si, R. Yu, and E. Abrahams, High-temperature superconductivity in iron pnictides and chalcogenides, *Nat. Rev. Mater.* **1**, 16017 (2016).
- [9] N. Ni, S. Nandi, A. Kreyssig, A. I. Goldman, E. D. Mun, S. L. Bud'ko, and P. C. Canfield, First-order structural phase transition in CaFe_2As_2 , *Phys. Rev. B* **78**, 014523 (2008).
- [10] A. I. Goldman, D. N. Argyriou, B. Ouladdiaf, T. Chatterji, A. Kreyssig, S. Nandi, N. Ni, S. L. Bud'ko, P. C. Canfield, and R. J. McQueeney, Lattice and magnetic instabilities in CaFe_2As_2 : A single-crystal neutron diffraction study, *Phys. Rev. B* **78**, 100506 (2008).
- [11] K.-Y. Choi, D. Wulferding, P. Lemmens, N. Ni, S. L. Bud'ko, and P. C. Canfield, Lattice and electronic anomalies of CaFe_2As_2 studied by Raman spectroscopy, *Phys. Rev. B* **78**, 212503 (2008).
- [12] M. A. Tanatar, N. Ni, G. D. Samolyuk, S. L. Bud'ko, P. C. Canfield, and R. Prozorov, Resistivity anisotropy of $A\text{Fe}_2\text{As}_2$ ($A = \text{Ca}, \text{Sr}, \text{Ba}$): Direct versus Montgomery technique measurements, *Phys. Rev. B* **79**, 134528 (2009).
- [13] M. A. Tanatar, E. C. Blomberg, A. Kreyssig, M. G. Kim, N. Ni, A. Thaler, S. L. Bud'ko, P. C. Canfield, A. I. Goldman, I. I. Mazin, and R. Prozorov, Uniaxial-strain mechanical detwinning of CaFe_2As_2 and BaFe_2As_2 crystals: Optical and transport study, *Phys. Rev. B* **81**, 184508 (2010).
- [14] P. C. Canfield, S. L. Bud'ko, N. Ni, A. Kreyssig, A. I. Goldman, R. J. McQueeney, M. S. Torikachvili, D. N. Argyriou, G. Luke, and W. Yu, Structural, magnetic and superconducting phase transitions in CaFe_2As_2 under ambient and applied pressure, *Physica C* **469**, 404 (2009).
- [15] S. Ran, S. L. Bud'ko, D. K. Pratt, A. Kreyssig, M. G. Kim, M. J. Kramer, D. H. Ryan, W. N. Rowan-Weetaluktuk, Y. Furukawa, B. Roy, A. I. Goldman, and P. C. Canfield, Stabilization of an ambient-pressure collapsed tetragonal phase in CaFe_2As_2 and tuning of the orthorhombic-antiferromagnetic transition temperature by over 70 K via control of nanoscale precipitates, *Phys. Rev. B* **83**, 144517 (2011).
- [16] A. Kreyssig, M. A. Green, Y. Lee, G. D. Samolyuk, P. Zajdel, J. W. Lynn, S. L. Bud'ko, M. S. Torikachvili, N. Ni, S. Nandi, J. B. Leão, S. J. Poulton, D. N. Argyriou, B. N. Harmon, R. J. McQueeney, P. C. Canfield, and A. I. Goldman, Pressure-induced volume-collapsed tetragonal phase of CaFe_2As_2 as seen via neutron scattering, *Phys. Rev. B* **78**, 184517 (2008).
- [17] A. I. Goldman, A. Kreyssig, K. Prokeš, D. K. Pratt, D. N. Argyriou, J. W. Lynn, S. Nandi, S. A. J. Kimber, Y. Chen, Y. B. Lee, G. Samolyuk, J. B. Leão, S. J. Poulton, S. L. Bud'ko, N. Ni, P. C. Canfield, B. N. Harmon, and R. J. McQueeney, Lattice collapse and quenching of magnetism in CaFe_2As_2 under pressure: A single-crystal neutron and x-ray diffraction investigation, *Phys. Rev. B* **79**, 024513 (2009).
- [18] M. Danura, K. Kudo, Y. Oshiro, S. Araki, T. C. Kobayashi, and M. Nohara, Interplay of Superconductivity and

- Fermi-Liquid Transport in Rh-Doped CaFe_2As_2 with Lattice-Collapse Transition, *J. Phys. Soc. Jpn.* **80**, 103701 (2011).
- [19] S. Kasahara, T. Shibauchi, K. Hashimoto, Y. Nakai, H. Ikeda, T. Terashima, and Y. Matsuda, Abrupt recovery of Fermi-liquid transport following the collapse of the c axis in $\text{CaFe}_2(\text{As}_{1-x}\text{P}_x)_2$ single crystals, *Phys. Rev. B* **83**, 060505(R) (2011).
- [20] S. R. Saha, N. P. Butch, T. Drye, J. Magill, S. Ziemak, K. Kirshenbaum, P. Y. Zavalij, J. W. Lynn, and J. Paglione, Structural collapse and superconductivity in rare-earth-doped CaFe_2As_2 , *Phys. Rev. B* **85**, 024525 (2012).
- [21] J. R. Jeffries, N. P. Butch, K. Kirshenbaum, S. R. Saha, G. Samudrala, S. T. Weir, Y. K. Vohra, and J. Paglione, Suppression of magnetism and development of superconductivity within the collapsed tetragonal phase of $\text{Ca}_{0.67}\text{Sr}_{0.33}\text{Fe}_2\text{As}_2$ under pressure, *Phys. Rev. B* **85**, 184501 (2012).
- [22] M. S. Torikachvili, S. L. Bud'ko, N. Ni, and P. C. Canfield, Pressure Induced Superconductivity in CaFe_2As_2 , *Phys. Rev. Lett.* **101**, 057006 (2008).
- [23] M. S. Torikachvili, S. L. Bud'ko, N. Ni, and P. C. Canfield, Effect of pressure on the structural phase transition and superconductivity in $(\text{Ba}_{1-x}\text{K}_x)\text{Fe}_2\text{As}_2$ ($x = 0$ and 0.45) and SrFe_2As_2 single crystals, *Phys. Rev. B* **78**, 104527 (2008).
- [24] H. Lee, E. Park, T. Park, V. A. Sidorov, F. Ronning, E. D. Bauer, and J. D. Thompson, Pressure-induced superconducting state of antiferromagnetic CaFe_2As_2 , *Phys. Rev. B* **80**, 024519 (2009).
- [25] P. M. Shirage, K. Miyazawa, H. Kito, H. Eisaki, and A. Iyo, Superconductivity at 26 K in $(\text{Ca}_{1-x}\text{Na}_x)\text{Fe}_2\text{As}_2$, *Appl. Phys. Express* **1**, 081702 (2008).
- [26] S. R. Saha, N. P. Butch, K. Kirshenbaum, and J. Paglione, Evolution of bulk superconductivity in SrFe_2As_2 with Ni substitution, *Phys. Rev. B* **79**, 224519 (2009).
- [27] S. L. Bud'ko, S. Ran, and P. C. Canfield, Thermal expansion of CaFe_2As_2 : Effect of cobalt doping and postgrowth thermal treatment, *Phys. Rev. B* **88**, 064513 (2013).
- [28] T. Okada, H. Ogino, H. Yakita, A. Yamamoto, K. Kishio, and J. Shimoyama, Effects of post-annealing and cobalt co-doping on superconducting properties of $(\text{Ca,Pr})\text{Fe}_2\text{As}_2$ single crystals, *Physica C* **505**, 1 (2014).
- [29] D. M. Wang, X. C. Shangguan, and J. B. He, Superconductivity at 35.5 K in K-Doped CaFe_2As_2 , *J. Supercond. Nov. Magn.* **26**, 2121 (2013).
- [30] K. Kudo, K. Iba, M. Takasuga, Y. Kitahama, J. Matsumura, M. Danura, Y. Nogami, and M. Nohara, Emergence of superconductivity at 45 K by lanthanum and phosphorus co-doping of CaFe_2As_2 , *Sci. Rep.* **3**, 1478 (2013).
- [31] M. Tegel, M. Rotter, V. Weiß, F. M. Schappacher, R. Pöttgen, and D. Johrendt, Structural and magnetic phase transitions in the ternary iron arsenides SrFe_2As_2 and EuFe_2As_2 , *J. Phys.: Condens. Matter* **20**, 452201 (2008).
- [32] J. Zhao, W. Ratcliff, J. W. Lynn, G. F. Chen, J. L. Luo, N. L. Wang, J. Hu, and P. Dai, Spin and lattice structures of single-crystalline SrFe_2As_2 , *Phys. Rev. B* **78**, 140504 (2008).
- [33] E. C. Blomberg, M. A. Tanatar, A. Kreyssig, N. Ni, A. Thaler, R. Hu, S. L. Bud'ko, P. C. Canfield, A. I. Goldman, and R. Prozorov, In-plane anisotropy of electrical resistivity in strain-detwinned SrFe_2As_2 , *Phys. Rev. B* **83**, 134505 (2011).
- [34] K. Sasmal, B. Lv, B. Lorenz, A. M. Guloy, F. Chen, Y.-Y. Xue, and C.-W. Chu, Superconducting Fe-Based Compounds $(\text{A}_{1-x}\text{Sr}_x)\text{Fe}_2\text{As}_2$ with $A = \text{K}$ and Cs with Transition Temperatures up to 37 K, *Phys. Rev. Lett.* **101**, 107007 (2008).
- [35] G.-F. Chen, Z. Li, G. Li, W.-Z. Hu, J. Dong, J. Zhou, X.-D. Zhang, P. Zheng, N.-L. Wang, and J.-L. Luo, Superconductivity in hole-doped $(\text{Sr}_{1-x}\text{K}_x)\text{Fe}_2\text{As}_2$, *Chin. Phys. Lett.* **25**, 3403 (2008).
- [36] T. Goko, A. A. Aczel, E. Baggio-Saitovitch, S. L. Bud'ko, P. C. Canfield, J. P. Carlo, G. F. Chen, Pengcheng Dai, A. C. Hamann, W. Z. Hu, H. Kageyama, G. M. Luke, J. L. Luo, B. Nachumi, N. Ni, D. Reznik, D. R. Sanchez-Candela, A. T. Savici, K. J. Sikes, N. L. Wang, C. R. Wiebe, T. J. Williams, T. Yamamoto, W. Yu, and Y. J. Uemura, Superconducting state coexisting with a phase-separated static magnetic order in $(\text{Ba,K})\text{Fe}_2\text{As}_2$, $(\text{Sr,Na})\text{Fe}_2\text{As}_2$, and CaFe_2As_2 , *Phys. Rev. B* **80**, 024508 (2009).
- [37] H. L. Shi, H. X. Yang, H. F. Tian, J. B. Lu, Z. W. Wang, Y. B. Qin, Y. J. Song, and J. Q. Li, Structural properties and superconductivity of $\text{SrFe}_2\text{As}_{2-x}\text{P}_x$ and $(0.0 \leq x \leq 1.0)$ and $\text{CaFe}_2\text{As}_{2-y}\text{P}_y$ ($0.0 \leq y \leq 0.3$), *J. Phys.: Condens. Matter* **22**, 125702 (2010).
- [38] P. L. Alireza, Y. T. C. Ko, J. Gillett, C. M. Petrone, J. M. Cole, S. E. Sebastian, and G. G. Lonzarich, Superconductivity up to 29 K in SrFe_2As_2 and BaFe_2As_2 at high pressures, *J. Phys.: Condens. Matter* **21**, 012208 (2009).
- [39] K. Kitagawa, N. Katayama, H. Gotou, T. Yagi, K. Ohgushi, T. Matsumoto, Y. Uwatoko, and M. Takigawa, Spontaneous Formation of a Superconducting and Antiferromagnetic Hybrid State in SrFe_2As_2 under High Pressure, *Phys. Rev. Lett.* **103**, 257002 (2009).
- [40] M. Rotter, M. Tegel, D. Johrendt, I. Schellenberg, W. Hermes, and R. Pöttgen, Spin-density-wave anomaly at 140 K in the ternary iron arsenide BaFe_2As_2 , *Phys. Rev. B* **78**, 020503(R) (2008).
- [41] F. Ishikawa, N. Eguchi, M. Kodama, K. Fujimaki, M. Einaga, A. Ohmura, A. Nakayama, A. Mitsuda, and Y. Yamada, Zero-resistance superconducting phase in BaFe_2As_2 under high pressure, *Phys. Rev. B* **79**, 172506 (2009).
- [42] E. Colombier, S. L. Bud'ko, N. Ni, and P. C. Canfield, Complete pressure-dependent phase diagrams for SrFe_2As_2 and BaFe_2As_2 , *Phys. Rev. B* **79**, 224518 (2009).
- [43] T. Yamazaki, N. Takeshita, R. Kobayashi, H. Fukazawa, Y. Kohori, K. Kihou, C.-H. Lee, H. Kito, A. Iyo, and H. Eisaki, Appearance of pressure-induced superconductivity in BaFe_2As_2 under hydrostatic conditions and its extremely high sensitivity to uniaxial stress, *Phys. Rev. B* **81**, 224511 (2010).
- [44] A. S. Sefat, R. Jin, M. A. McGuire, B. C. Sales, D. J. Singh, and D. Mandrus, Superconductivity at 22 K in Co-Doped BaFe_2As_2 Crystals, *Phys. Rev. Lett.* **101**, 117004 (2008).
- [45] N. Ni, M. E. Tillman, J.-Q. Yan, A. Kracher, S. T. Hannahs, S. L. Bud'ko, and P. C. Canfield, Effects of Co substitution on thermodynamic and transport properties and anisotropic H_{c2} in $\text{Ba}(\text{Fe}_{1-x}\text{Co}_x)_2\text{As}_2$ single crystals, *Phys. Rev. B* **78**, 214515 (2008).
- [46] J.-H. Chu, J. G. Analytis, C. Kucharczyk, and I. R. Fisher, Determination of the phase diagram of the electron-doped superconductor $\text{Ba}(\text{Fe}_{1-x}\text{Co}_x)_2\text{As}_2$, *Phys. Rev. B* **79**, 014506 (2009).
- [47] P. C. Canfield, S. L. Bud'ko, N. Ni, J. Q. Yan, and A. Kracher, Decoupling of the superconducting and magnetic/structural phase transitions in electron-doped BaFe_2As_2 , *Phys. Rev. B* **80**, 060501 (2009).

- [48] M. Rotter, M. Tegel, and D. Johrendt, Superconductivity at 38 K in the Iron Arsenide $(\text{Ba}_{1-x}\text{K}_x)\text{Fe}_2\text{As}_2$, *Phys. Rev. Lett.* **101**, 107006 (2008).
- [49] N. Ni, S. L. Bud'ko, A. Kreyssig, S. Nandi, G. E. Rustan, A. I. Goldman, S. Gupta, J. D. Corbett, A. Kracher, and P. C. Canfield, Anisotropic thermodynamic and transport properties of single-crystalline $\text{Ba}_{1-x}\text{K}_x\text{Fe}_2\text{As}_2$ ($x = 0$ and 0.45), *Phys. Rev. B* **78**, 014507 (2008).
- [50] H. Chen, Y. Ren, Y. Qiu, Wei Bao, R. H. Liu, G. Wu, T. Wu, Y. L. Xie, X. F. Wang, Q. Huang, and X. H. Chen, Coexistence of the spin-density wave and superconductivity in $\text{Ba}_{1-x}\text{K}_x\text{Fe}_2\text{As}_2$, *Europhys. Lett.* **85**, 17006 (2009).
- [51] Shuai Jiang, Hui Xing, Guofang Xuan, Cao Wang, Zhi Ren, C. Feng, J. Dai, Z. Xu, and G. Cao, Superconductivity up to 30 K in the vicinity of the quantum critical point in $\text{BaFe}_2(\text{As}_{1-x}\text{P}_x)_2$, *J. Phys.: Condens. Matter* **21**, 382203 (2009).
- [52] F. Rullier-Albenque, D. Colson, A. Forget, P. Thuéry, and S. Poissonnet, Hole and electron contributions to the transport properties of $\text{Ba}(\text{Fe}_{1-x}\text{Ru}_x)_2\text{As}_2$ single crystals, *Phys. Rev. B* **81**, 224503 (2010).
- [53] A. Thaler, N. Ni, A. Kracher, J. Q. Yan, S. L. Bud'ko, and P. C. Canfield, Physical and magnetic properties of $\text{Ba}(\text{Fe}_{1-x}\text{Ru}_x)_2\text{As}_2$ single crystals, *Phys. Rev. B* **82**, 014534 (2010).
- [54] Y. Nakai, T. Iye, S. Kitagawa, K. Ishida, H. Ikeda, S. Kasahara, H. Shishido, T. Shibauchi, Y. Matsuda, and T. Terashima, Unconventional Superconductivity and Antiferromagnetic Quantum Critical Behavior in the Isovalent-Doped $\text{BaFe}_2(\text{As}_{1-x}\text{P}_x)_2$, *Phys. Rev. Lett.* **105**, 107003 (2010).
- [55] S. Kasahara, T. Shibauchi, K. Hashimoto, K. Ikada, S. Tonegawa, R. Okazaki, H. Shishido, H. Ikeda, H. Takeya, K. Hirata, T. Terashima, and Y. Matsuda, Evolution from non-Fermi- to Fermi-liquid transport via isovalent doping in $\text{BaFe}_2(\text{As}_{1-x}\text{P}_x)_2$ superconductors, *Phys. Rev. B* **81**, 184519(R) (2010).
- [56] C. Cao, P. J. Hirschfeld, and H.-P. Cheng, Proximity of antiferromagnetism and superconductivity in $\text{LaFeAsO}_{1-x}\text{F}_x$: Effective Hamiltonian from ab initio studies, *Phys. Rev. B* **77**, 220506 (2008).
- [57] X. Dai, Z. Fang, Y. Zhou, and F.-C. Zhang, Even Parity, Orbital Singlet, and Spin Triplet Pairing for Superconducting $\text{LaFeAsO}_{1-x}\text{F}_x$, *Phys. Rev. Lett.* **101**, 057008 (2008).
- [58] F. Ma, W. Ji, J. Hu, Z.-Y. Lu, and T. Xiang, First-Principles Calculations of the Electronic Structure of Tetragonal α -FeTe and α -FeSe Crystals: Evidence for a Bicollinear Antiferromagnetic Order, *Phys. Rev. Lett.* **102**, 177003 (2009).
- [59] M. P. Allan, K. Lee, A. W. Rost, M. H. Fischer, F. Masseur, K. Kihou, C.-H. Lee, A. Iyo, H. Eisaki, T.-M. Chuang, J. C. Davis, and E.-A. Kim, Identifying the ‘fingerprint’ of antiferromagnetic spin fluctuations in iron pnictide superconductors, *Nat. Phys.* **11**, 177 (2014).
- [60] L. Boeri, O. V. Dolgov, and A. A. Golubov, Is $\text{LaFeAsO}_{1-x}\text{F}_x$ an Electron-Phonon Superconductor? *Phys. Rev. Lett.* **101**, 026403 (2008).
- [61] A. Akrap, J. J. Tu, L. J. Li, G. H. Cao, Z. A. Xu, and C. C. Homes, Infrared phonon anomaly in BaFe_2As_2 , *Phys. Rev. B* **80**, 180502 (2009).
- [62] D. Wu, N. Barišić, N. Drichko, S. Kaiser, A. Faridian, M. Dressel, S. Jiang, Z. Ren, L. J. Li, G. H. Cao, Z. A. Xu, H. S. Jeevan, and P. Gegenwart, Effects of magnetic ordering on dynamical conductivity: Optical investigations of EuFe_2As_2 single crystals, *Phys. Rev. B* **79**, 155103 (2009).
- [63] M. Nakajima, T. Liang, S. Ishida, Y. Tomioka, K. Kihou, C. H. Lee, A. Iyo, H. Eisaki, T. Kakeshita, T. Ito, and S. Uchida, Unprecedented anisotropic metallic state in undoped iron arsenide BaFe_2As_2 revealed by optical spectroscopy, *Proc. Natl. Acad. Sci. USA* **108**, 12238 (2011).
- [64] A. A. Schafgans, B. C. Pursley, A. D. LaForge, A. S. Sefat, D. Mandrus, and D. N. Basov, Phonon splitting and anomalous enhancement of infrared-active modes in BaFe_2As_2 , *Phys. Rev. B* **84**, 052501 (2011).
- [65] A. Charnukha, D. Pröpper, T. I. Larkin, D. L. Sun, Z. W. Li, C. T. Lin, T. Wolf, B. Keimer, and A. V. Boris, Spin-density-wave-induced anomalies in the optical conductivity of $A\text{Fe}_2\text{As}_2$, ($A = \text{Ca}, \text{Sr}, \text{Ba}$) single-crystalline iron pnictides, *Phys. Rev. B* **88**, 184511 (2013).
- [66] R. H. Liu, T. Wu, G. Wu, H. Chen, X. F. Wang, Y. L. Xie, J. J. Ying, Y. J. Yan, Q. J. Li, B. C. Shi, W. S. Chu, Z. Y. Wu, and X. H. Chen, A large iron isotope effect in $\text{SmFeAsO}_{1-x}\text{F}_x$ and $\text{Ba}_{1-x}\text{K}_x\text{Fe}_2\text{As}_2$, *Nature (London)* **459**, 64 (2009).
- [67] Y. M. Dai, Ana Akrap, S. L. Bud'ko, P. C. Canfield, and C. C. Homes, Optical properties of $A\text{Fe}_2\text{As}_2$ ($A = \text{Ca}, \text{Sr}, \text{and Ba}$) single crystals, *Phys. Rev. B* **94**, 195142 (2016).
- [68] J.-Q. Yan, A. Kreyssig, S. Nandi, N. Ni, S. L. Bud'ko, A. Kracher, R. J. McQueeney, R. W. McCallum, T. A. Lograsso, A. I. Goldman, and P. C. Canfield, Structural transition and anisotropic properties of single-crystalline SrFe_2As_2 , *Phys. Rev. B* **78**, 024516 (2008).
- [69] C. C. Homes, M. Reedyk, D. A. Crandles, and T. Timusk, Technique for measuring the reflectance of irregular, submillimeter-sized samples, *Appl. Opt.* **32**, 2976 (1993).
- [70] M. Dressel and G. Grüner, *Electrodynamics of Solids* (Cambridge University Press, Cambridge, 2001).
- [71] T. Yildirim, Origin of the 150-K Anomaly in LaFeAsO : Competing Antiferromagnetic Interactions, Frustration, and a Structural Phase Transition, *Phys. Rev. Lett.* **101**, 057010 (2008).
- [72] G. Wu, H. Chen, T. Wu, Y. L. Xie, Y. J. Yan, R. H. Liu, X. F. Wang, J. J. Ying, and X. H. Chen, Different resistivity response to spin-density wave and superconductivity at 20 K in $\text{Ca}_{1-x}\text{Na}_x\text{Fe}_2\text{As}_2$, *J. Phys.: Condens. Matter* **20**, 422201 (2008).
- [73] A. Damascelli, Optical Spectroscopy of Quantum Spin Systems, Ph.D. thesis, University of Groningen, 1996, p. 21.
- [74] A. Kuzmenko, *Software REFFIT, Manual* (2014), p. 64, <https://sites.google.com/site/reffitprogram/home>.
- [75] D. Wu, N. Barišić, P. Kallina, A. Faridian, B. Gorshunov, N. Drichko, L. J. Li, X. Lin, G. H. Cao, Z. A. Xu, N. L. Wang, and M. Dressel, Optical investigations of the normal and superconducting states reveal two electronic subsystems in iron pnictides, *Phys. Rev. B* **81**, 100512(R) (2010).
- [76] D. J. Singh, *Planewaves, Pseudopotentials and the LAPW Method* (Kluwer Academic, Boston, 1994).
- [77] D. Singh, Ground-state properties of lanthanum: Treatment of extended-core states, *Phys. Rev. B* **43**, 6388 (1991).
- [78] P. Blaha, K. Schwarz, G. K. H. Madsen, D. Kvasnicka, and J. Luitz, WIEN2k, *An Augmented Plane Wave Plus Local Orbitals Program for Calculating Crystal Properties* (Techn. Universität Wien, Austria, 2001).

- [79] T. Yildirim, Strong Coupling of the Fe-Spin State and the As-As Hybridization in Iron-Pnictide Superconductors from First-Principle Calculations, *Phys. Rev. Lett.* **102**, 037003 (2009).
- [80] M. Zbiri, H. Schober, M. R. Johnson, S. Rols, R. Mittal, Y. Su, M. Rotter, and D. Johrendt, *Ab initio* lattice dynamics simulations and inelastic neutron scattering spectra for studying phonons in BaFe₂As₂: Effect of structural phase transition, structural relaxation, and magnetic ordering, *Phys. Rev. B* **79**, 064511 (2009).
- [81] A. P. Litvinchuk, V. G. Hadjiev, M. N. Iliev, B. Lv, A. M. Guloy, and C. W. Chu, Raman-scattering study of K_xSr_{1-x}Fe₂As₂ ($x = 0.0, 0.4$), *Phys. Rev. B* **78**, 060503(R) (2008).
- [82] L. Chauvière, Y. Gallais, M. Cazayous, A. Sacuto, M. A. Méasson, D. Colson, and A. Forget, Doping dependence of the lattice dynamics in Ba(Fe_{1-x}Co_x)₂As₂ studied by Raman spectroscopy, *Phys. Rev. B* **80**, 094504 (2009).
- [83] L. Chauvière, Y. Gallais, M. Cazayous, M. A. Méasson, A. Sacuto, D. Colson, and A. Forget, Raman scattering study of spin-density-wave order and electron-phonon coupling in Ba(Fe_{1-x}Co_x)₂As₂, *Phys. Rev. B* **84**, 104508 (2011).
- [84] K. Parlinski, *Software* PHONON (2003).
- [85] M. Sandoghchi, H. Khosroabadi, H. Almasi, and M. Akhavan, Electronic and phonon structures of BaFe₂As₂ superconductor by *Ab-initio* density functional theory, *J. Supercond. Nov. Magn.* **26**, 93 (2013).
- [86] C. C. Homes, Y. M. Dai, J. Schneeloch, R. D. Zhong, and G. D. Gu, Phonon anomalies in some iron telluride materials, *Phys. Rev. B* **93**, 125135 (2016).
- [87] L. Boeri, M. Calandra, I. I. Mazin, O. V. Dolgov, and F. Mauri, Effects of magnetism and doping on the electron-phonon coupling in BaFe₂As₂, *Phys. Rev. B* **82**, 020506(R) (2010).
- [88] P. G. Klemens, Anharmonic decay of optical phonons, *Phys. Rev.* **148**, 845 (1966).
- [89] J. Menéndez and M. Cardona, Temperature dependence of the first-order Raman scattering by phonons in Si, Ge, and α -Sn: Anharmonic effects, *Phys. Rev. B* **29**, 2051 (1984).
- [90] E. Dowty, *Software* VIBRATZ (Shape Software, Kingsport, TN, 2001).
- [91] M. Kofu, Y. Qiu, Wei Bao, S.-H. Lee, S. Chang, T. Wu, G. Wu, and X. H. Chen, Neutron scattering investigation of the magnetic order in single crystalline BaFe₂As₂, *New J. Phys.* **11**, 055001 (2009).
- [92] A. Dusza, A. Lucarelli, F. Pfuner, J.-H. Chu, I. R. Fisher, and L. Degiorgi, Anisotropic charge dynamics in detwinned Ba(Fe_{1-x}Co_x)₂As₂, *Europhys. Lett.* **93**, 37002 (2011).
- [93] A. Dusza, A. Lucarelli, A. Sanna, S. Massidda, J.-H. Chu, I. R. Fisher, and L. Degiorgi, Anisotropic in-plane optical conductivity in detwinned Ba(Fe_{1-x}Co_x)₂As₂, *New J. Phys.* **14**, 023020 (2012).
- [94] C. C. Homes, A. W. McConnell, B. P. Clayman, D. A. Bonn, R. Liang, W. N. Hardy, M. Inoue, H. Negishi, P. Fournier, and R. L. Greene, Phonon Screening in High-Temperature Superconductors, *Phys. Rev. Lett.* **84**, 5391 (2000).
- [95] Tao Li, Orbital degeneracy and the microscopic model of the FeAs plane in the iron-based superconductors, *J. Phys.: Condens. Matter* **20**, 425203 (2008).
- [96] O. K. Andersen and L. Boeri, On the multi-orbital band structure and itinerant magnetism of iron-based superconductors, *Ann. Phys.* **523**, 8 (2011).
- [97] T. Shimojima, K. Ishizaka, Y. Ishida, N. Katayama, K. Ohgushi, T. Kiss, M. Okawa, T. Togashi, X.-Y. Wang, C.-T. Chen, S. Watanabe, R. Kadota, T. Oguchi, A. Chainani, and S. Shin, Orbital-Dependent Modifications of Electronic Structure across the Magnetostructural Transition in BaFe₂As₂, *Phys. Rev. Lett.* **104**, 057002 (2010).
- [98] P. Richard, K. Nakayama, T. Sato, M. Neupane, Y.-M. Xu, J. H. Bowen, G. F. Chen, J. L. Luo, N. L. Wang, X. Dai, Z. Fang, H. Ding, and T. Takahashi, Observation of Dirac Cone Electronic Dispersion in BaFe₂As₂, *Phys. Rev. Lett.* **104**, 137001 (2010).
- [99] Z. P. Yin, K. Haule, and G. Kotliar, Magnetism and charge dynamics in iron pnictides, *Nat. Phys.* **7**, 294 (2011).
- [100] W. Lv, J. Wu, and P. Phillips, Orbital ordering induces structural phase transition and the resistivity anomaly in iron pnictides, *Phys. Rev. B* **80**, 224506 (2009).
- [101] C.-C. Lee, W.-G. Yin, and W. Ku, Ferro-Orbital Order and Strong Magnetic Anisotropy in the Parent Compounds of Iron-Pnictide Superconductors, *Phys. Rev. Lett.* **103**, 267001 (2009).
- [102] F. Krüger, S. Kumar, J. Zaanen, and J. van den Brink, Spin-orbital frustrations and anomalous metallic state in iron-pnictide superconductors, *Phys. Rev. B* **79**, 054504 (2009).
- [103] B. Valenzuela, E. Bascones, and M. J. Calderón, Conductivity Anisotropy in the Antiferromagnetic State of Iron Pnictides, *Phys. Rev. Lett.* **105**, 207202 (2010).
- [104] P. Dai, J. Hu, and E. Dagotto, Magnetism and its microscopic origin in iron-based high-temperature superconductors, *Nat. Phys.* **8**, 709 (2012).
- [105] S. Liang, A. Moreo, and E. Dagotto, Nematic State of Pnictides Stabilized by Interplay between Spin, Orbital, and Lattice Degrees of Freedom, *Phys. Rev. Lett.* **111**, 047004 (2013).
- [106] R. M. Fernandes, A. V. Chubukov, and J. Schmalian, What drives nematic order in iron-based superconductors? *Nat. Phys.* **10**, 97 (2014).
- [107] A. V. Chubukov, M. Khodas, and R. M. Fernandes, Magnetism, Superconductivity, and Spontaneous Orbital Order in Iron-Based Superconductors: Which Comes First and Why? *Phys. Rev. X* **6**, 041045 (2016).